Strength of correlations in a silver-based cuprate analog

Riccardo Piombo [1] Daniel Jezierski [2] Henrique Perin Martins,[3] Tomasz Jaroń [2,4] Maria N. Gastiasoro,[5]
Paolo Barone [6] Kamil Tokár [7,8] Przemysław Piekarz [9] Mariana Derzsi [7] Zoran Mazej [10]
Miguel Abbate,[3] Wojciech Grochala [2,*] and José Lorenzana [5,†]

[1]*Dipartimento di Fisica, Università di Roma "La Sapienza," 00185 Rome, Italy*
[2]*Center of New Technologies, University of Warsaw, Zwirki i Wigury 93, 02089 Warsaw, Poland*
[3]*Departamento de Física, Universidade Federal do Paraná, Caixa Postal 19044, 81531-990 Curitiba, PR, Brazil*
[4]*Faculty of Chemistry, University of Warsaw, Pasteura 1, 02-089 Warsaw, Poland*
[5]*ISC-CNR Institute for Complex Systems, Consiglio Nazionale delle Ricerche,*
Dipartimento di Fisica, Università di Roma "La Sapienza," 00185 Rome, Italy
[6]*SPIN-CNR Institute for Superconducting and other Innovative Materials, Consiglio Nazionale delle Ricerche,*
Area della Ricerca di Tor Vergata, Via del Fosso del Cavaliere 100, 00133 Rome, Italy
[7]*Advanced Technologies Research Institute, Faculty of Materials Science and Technology in Trnava,*
Slovak University of Technology in Bratislava, Jána Bottu 25, 917 24 Bratislava, Trnava, Slovakia
[8]*Institute of Physics, Slovak Academy of Sciences, Dúbravská cesta 9, 845 11 Bratislava, Slovakia*
[9]*Institute of Nuclear Physics, Polish Academy of Sciences, Radzikowskiego 152, 31342 Kraków, Poland*
[10]*Jožef Stefan Institute, Department of Inorganic Chemistry and Technology, Jamova cesta 39, 1000 Ljubljana, Slovenia*

AgF_2 has been proposed as a cuprate analog, which requires strong correlation and marked covalence. On the other hand, fluorides are usually quite ionic, and $4d$ transition metals tend to be less correlated than their $3d$ counterparts, which calls for further scrutiny. We combine valence band photoemission and Auger-Meitner spectroscopy of AgF and AgF_2 together with computations in small clusters to estimate values of the Ag $4d$ Coulomb interaction U_{4d} and charge-transfer energy Δ_{pd}. Based on these values, AgF_2 can be classified as a charge-transfer correlated insulator according to the Zaanen-Sawatzky-Allen classification scheme. Thus, we confirm that the material is a cuprate analog from the point of view of correlations, suggesting that it should become a high-temperature superconductor if metallization is achieved by doping. We present also a computation of the Hubbard U in density functional "$+U$" methods and discuss its relation to the Hubbard U in spectroscopies.

I. INTRODUCTION

Since the discovery of high-T_c superconductivity in copper oxides, there has been intense effort to find compounds with similar characteristics but different ions [1]. Such materials can provide insights in understanding unconventional high-T_c superconductivity and may lead to new applications. Iron pnictides and chalcogenides share similarities with cuprates in the phase diagram but have prominent multiorbital physics absent in cuprates. A recent step forward [2] is the discovery of superconductivity in Sr-doped $NdNiO_2$, which in the undoped phase has formally the same d^9 configuration as cuprates. However, differently from cuprates, parent phases seem to be metallic and nonmagnetic [3] and the splitting between transition metal d and O p levels seems to be significantly larger [4,5]. Also, the T_c value for this material is quite low, in stark contrast with cuprates.

Another interesting nearest neighbor of Cu in the periodic table is Ag; however, it has long been known that the charge-transfer gap in AgO is formally negative [6] and indeed AgO is not even magnetic. A positive charge-transfer energy can be recovered, replacing the oxygen ion with the only element that can oxidize it, namely, fluorine [7]. AgF_2 is a layered material with similar topology to that of cuprates but larger buckling of planes which should depress the superexchange J. Experiments show that J reaches 70% of a typical cuprate; moreover, flattening of the AgF_2 sheets would blast the J value way above those measured for cuprates [8,9]. From the theory side, estimates of hopping integrals between the metal and ligand for AgF_2 are very similar to known values in cuprates [8,10–13].

A major open question to establish the similarities between the two families is the strength of the intraorbital Coulomb repulsion in silver, U_{4d}. In general, it is expected that the more diffuse character of $4d$ with respect to $3d$ orbitals will make correlations less important. It has been argued [8] that this may be partially compensated by less efficient screening in AgF_2, as F^- is less polarizable than O^{2-}. Another important question is the magnitude of the charge-transfer energy, Δ_{pd},

*w.grochala@cent.uw.edu.pl
†jose.lorenzana@cnr.it

as fluorides are often very ionic compounds while cuprates are quite covalent. Recent optical and resonant inelastic x-ray scattering (RIXS) measurements show a larger fundamental gap and simultaneously a similar or even larger degree of covalence in AgF_2 than in cuprates [14]. This apparently paradoxical result was explained in terms of a large intersite Coulomb repulsion.

To further determine the relevant electronic parameters of AgF_2, here we present a high-energy spectroscopy study combining valence band x-ray photoemission spectroscopy (XPS) of AgF_2 (d^9) and its filled-shell partner AgF (d^{10}), Auger-Meitner spectroscopy of AgF, and cluster computations.

To determine the on-site repulsion directly from spectroscopic information, one needs to access an excited state with two holes on the transition metal (d^8). This is naturally achieved in closed-shell systems such as AgF by Auger-Meitner spectroscopy [15,16]. Thus, for this compound we obtained both Δ_{pd} and U_{4d} using also valence band XPS. While the AgF U_{4d} value can be taken as a reference, it would be desirable to have spectroscopic information directly on AgF_2. Valence band XPS does probe the d^8 state of AgF_2. Unfortunately, present experiments do not resolve directly d^8 satellites and the visible features do not allow for an accurate determination of parameters. Yet, we argue that the experiments impose enough constraints to classify the system as a strongly correlated charge-transfer insulator, confirming the analogy with cuprates.

II. EXPERIMENTAL SETUP

X-ray photoelectron spectra were measured using a custom-designed system made by SPECS (Berlin) with a loadlock connected to an MBraun LABSTAR glovebox filled with Ar (monitored O_2 and H_2O levels, typically <0.5 ppm). The spectra presented in this paper were recorded with the Al-Kα line (1486.74 eV, resolution 0.25 eV) at 32-mA emission current and 12.5-kV anode bias (400 W). A single crystal quartz mirror monochromator, the Phoibos 100 hemispherical analyzer (100-mm mean radius), and a delayline electron detection system (DLD 3636) were used for the measurements. Powder samples were loaded in a holder provided by SPECS via a glove box in argon atmosphere. The AgF_2 samples were sputtered with Ar^+ ions at 6 mA and 2 keV for 30 min before spectra acquisition. An electron flood gun FG 15/40 was used for the charge compensation of the AgF_2 samples. More details can be found in Ref. [17].

III. MODEL

For the cluster simulations, we considered a central Ag atom and six surrounding F atoms. Figure 1 shows the clusters used in gray and some extra surrounding atoms that are implicitly taken into account in the effective parameters defining the cluster Hamiltonian. For AgF the local symmetry is O_h which is well represented by an $(AgF_6)^{5-}$ cluster [Fig. 1(a)]. For AgF_2 the point-group symmetry at the Ag site is C_i (only inversion as nontrivial symmetry operation), thus we considered the distorted $(AgF_6)^{4-}$ cluster shown in Fig. 1(b). We considered five 4d orbitals which hybridize with
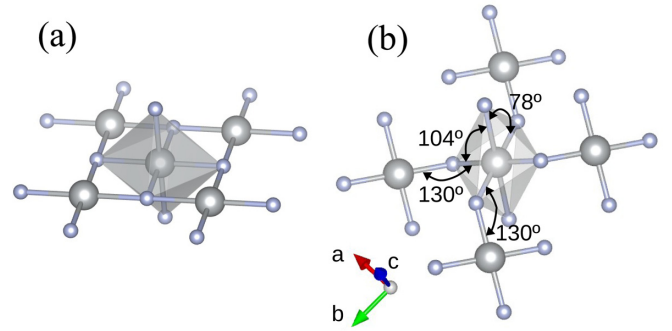

FIG. 1. AgF_6 clusters used in the computations (highlighted in gray) for AgF (a) and AgF_2 (b). In the case of AgF_2 we indicated some angles. Analogous angles in AgF are either 90° or 180°.

five symmetry adapted linear combinations of p orbitals from the neighboring F atoms, as in Ref. [14].

The cluster Hamiltonian in both cases reads

$$
\begin{aligned}
H = &\sum_\nu \varepsilon_{4d}^\nu d_\nu^\dagger d_\nu + \sum_\nu \varepsilon_P^\nu P_\nu^\dagger P_\nu \\
&+ \sum_\nu T_{pd}^\nu (d_\nu^\dagger P_\nu + P_\nu^\dagger d_\nu) \\
&+ \sum_{\substack{\nu_1, \nu_2 \\ \nu_3, \nu_4}} U^{(PP)}(\nu_1, \nu_2, \nu_3, \nu_4) P_{\nu_1}^\dagger P_{\nu_2}^\dagger P_{\nu_3} P_{\nu_4} \\
&+ \sum_{\substack{\nu_1, \nu_2 \\ \nu_3, \nu_4}} U^{(dd)}(\nu_1, \nu_2, \nu_3, \nu_4) d_{\nu_1}^\dagger d_{\nu_2}^\dagger d_{\nu_3} d_{\nu_4} \\
&+ \sum_{\nu_1, \nu_2} U_{pd} P_{\nu_1}^\dagger P_{\nu_1} d_{\nu_2}^\dagger d_{\nu_2}.
\end{aligned}
\tag{1}
$$

Here, $d_\nu^\dagger$ creates a hole in the 4d orbitals while $P_\nu^\dagger$ creates a hole in symmetry adapted combinations of F p orbitals. ν labels orbitals and spin quantum numbers. T_{pd}^ν are hybridization matrix elements between the localized d orbitals and the symmetry adapted P orbitals. In the following, we will use the notation "P character" to refer to the spectral weight in the symmetry adapted P basis.

The procedure to define the symmetry adapted orbitals for AgF_2 [Fig. 1(b)] is explained in Ref. [14]. Despite the low local C_i symmetry, the hybridization matrix elements with the P orbitals were found in density functional theory (DFT) [14] to be very close to matrix elements assuming D_{4h} symmetry and a Slater-Koster [18] parametrization with $T_{pd}^{x^2-y^2} = 2.76$ eV, which is in good agreement with typical values in cuprates (2.3–3.0 eV).

The diagonal energies ε_d^ν and ε_P^ν from DFT are shown in Table I. In contrast with the hybridization matrix elements, ε_P^ν values are very different to the ones obtained in D_{4h} symmetry. Thus, for the latter, symmetry constraints do not help to reduce the number of independent parameters. Furthermore, other problems preclude an accurate determination from first principles: First, ε_P^ν should also incorporate mean-field corrections to take into account interaction with the next shell of atoms which is not present in the cluster. Second, one expects that crystal field parameters will be more affected by self-interaction corrections than hybridization matrix

TABLE I. Crystal fields and hybridizations for AgF$_2$ from the DFT computations of Ref. [14]. We defined $\varepsilon_P^\nu = \Delta_{pd} + e_P^\nu$. All values are in eV. The last three columns are the expression for a planar cluster neglecting crystal fields in the d shell from Ref. [21].

ν	AgF$_2$ (C_i)			D_{4h}		
	ε_d^ν	e_P^ν	T_{pd}^ν	ε_d^ν	e_P^ν	T_{pd}
z^2	-0.25	0.32	1.51	0	$\frac{4}{5}T_{pp}$	$\frac{1}{\sqrt{3}}T_{pd}^{x^2-y^2}$
x^2-y^2	-0.28	-0.16	2.76	0	$-\frac{6}{5}T_{pp}$	$T_{pd}^{x^2-y^2}$
xy	0.34	-0.05	1.36	0	$\frac{4}{5}T_{pp}$	$\frac{1}{2}T_{pd}^{x^2-y^2}$
xz	0.09	-0.14	1.05	0	$-\frac{1}{5}T_{pp}$	$\frac{1}{2\sqrt{2}}T_{pd}^{x^2-y^2}$
yz	0.10	0.04	1.02	0	$-\frac{1}{5}T_{pp}$	$\frac{1}{2\sqrt{2}}T_{pd}^{x^2-y^2}$

elements. Indeed, crystal field splittings in DFT tend to be significantly smaller than in more accurate quantum chemistry methods [19,20]. In view of these difficulties, we also explored an *ad hoc* set of diagonal energies, as explained in Sec. IV C 2.

For AgF, the definition of the symmetry adapted orbitals is standard. The F-Ag hopping matrix element, $t_{pd} = T_{pd}^{x^2-y^2}/2$, has been shown to follow Andersen scaling [22] $t'_{pd} = t_{pd}(d/d')^4$ and $t_{pp} = t_{pp}(d/d')^2$ with d the distance between the involved atoms (see Supplementary Information to Ref. [8]). Thus, for AgF we adapted the hybridization matrix elements derived for AgF$_2$ with the Andersen scaling correction yielding $T_{pd}^{x^2-y^2} = 1.38$ eV and $T_{pp} = 0.29$ eV.

With these settings, a total of 20 electrons can be accommodated in the clusters for both fluorides. Stoichiometric AgF and AgF$_2$ correspond to configurations with zero ($N = 20$ electrons) and one hole, respectively ($N = 19$). We define the charge-transfer energy as the energy cost $\Delta_{pd} = E(d^{10}\underline{L}) - E(d^9)$ for $T_{pd}^\nu = 0$ with $\underline{L}$ denoting a hole in the ligand. The energies E are averages of the corresponding multiplets including the diagonal energies ε_d^ν and ε_P^ν.

When referring to the Hubbard U repulsion, it is important to specify which Hubbard interaction is meant. In the two-hole subspace $U^{(dd)}$ is a 45×45 matrix representing Coulomb repulsion on Ag. From the trace we can define the average interaction $\overline{U}_{dd} = F^0 - 2(F^2 + F^4)/63$, with F^k being the Slater-Condon integrals. Another important matrix element is the intraorbital repulsion, $U_{4d} \equiv U(^1A_{1g}) = F^0 + 4(F^2 + F^4)/49$, where the symmetry in parentheses corresponds to the d^8 state. The Auger process is dominated by a ^1G final state [6] so it is useful to define also $U(^1G) = F^0 + (36F^2 + F^4)/441$.

F^2 and F^4 represent high multipole Coulomb interaction matrix elements and are weakly screened in solids. They can be obtained from other compounds with Ag^{2+} ions. We took $F^2 = 8.19$ eV and $F^4 = 6.80$ eV from Ref. [6]. On the other hand, F^0 is strongly screened in an environmentally dependent manner [23–26] and our goal is to determine it, or equivalently U_{4d}, in silver fluorides. The latter is a good estimate of the repulsion parameter in a generalized Emery model [27] to be used as a starting point of the theoretical description of correlation in AgF$_2$. Because of the d^9 nature of AgF$_2$, one expects that this model captures both the

intermediate-energy physics (excitons, optics, and magnetic interactions) as well as the low-energy physics.

On-site F and intersite Ag-F Coulomb repulsions can also be large in this system as F orbitals are more localized than O orbitals, so they were explicitly retained instead of absorbing them at a mean-field level as it is often done in cuprates. The repulsion in a single fluorine is described by a $U^{(pp)}$ matrix. For simplicity, we retained only one parameter, the monopole term of $U^{(pp)}$. This interaction was projected on the basis of symmetry adapted P orbitals, which resulted in the U^{PP} matrix as described in Appendix A. For U_{pd}, for simplicity, we also retained only the monopole term which leads straightforwardly to the expression in Eq. (1).

The valence band photoemission spectroscopy of AgF and AgF$_2$ was computed in terms of the one-hole spectral function of the cluster projected on d or P states, $A_{d/P}(\omega)$. This should be weighted with the atomic cross-section ratios which were taken from Ref. [28] (divided by the number of electrons in the shell). In the case of the Al-Kα source used in the present paper, one obtains $r = \sigma(\text{F}2p)/\sigma(\text{Ag}4d) = 0.05$.

Because the number of F per Ag is different in the cluster and the bulk compound, an additional correction is needed. In the ionic limit, the total integrated F p spectral weight per Ag atom corresponds to 12 states per AgF$_2$ and six states for AgF. Instead, in the clusters those weights are 10 in both cases corresponding to ten filled F orbitals. To take this into account, we computed the photoemission intensity as $I = A_d(\omega) + r(12/10)A_P(\omega)$ for AgF$_2$ and $I = A_d(\omega) + r(6/10)A_P(\omega)$ for AgF. In practice due to the smallness of r the intensity is dominated by the silver response. Following Ref. [29] we assumed that the Auger-Meitner spectrum is dominated by the two-hole spectral function in the singlet channel [6].

IV. RESULTS

A. Valence band photoemission of AgF

We now discuss the valence band photoemission spectrum of AgF, which is shown in Fig. 2. The experimental spectrum is close to previous published results [30]. Since AgF is a filled-shell system, the final state has only one hole which makes two-hole interactions irrelevant. In this case, for simplicity we follow Ref. [21] and fix $\varepsilon_{4d}^\nu = 0$ and $\varepsilon_P^\nu = \Delta_{pd}$. Using the hybridization determined above and varying Δ_{pd} we obtain excellent agreement with the experiment. A weak shoulder appears above 4 eV which is probably due to band structure effects not captured by the cluster computation.

The inset shows the removal spectral functions contributing to the line shape as explained above. The $d(p)$ spectral weight peaks near 5-eV (7.5-eV) binding energy and shows strong covalence [30]. Indeed, there is a sizable shoulder of the d spectral function at the peak of the p spectral function and vice versa. This is reflected also in the small value of the charge-transfer energy for this compound, $\Delta_{pd} = 1.2$ eV, and illustrates nicely that silver fluorides are exceptionally covalent [30] in contrast to most fluorides which are ionic.

B. Auger-Meitner spectroscopy of AgF

The above experiment sets the stage for Auger-Meitner *MNN* spectroscopy (hereafter Auger spectroscopy) in AgF
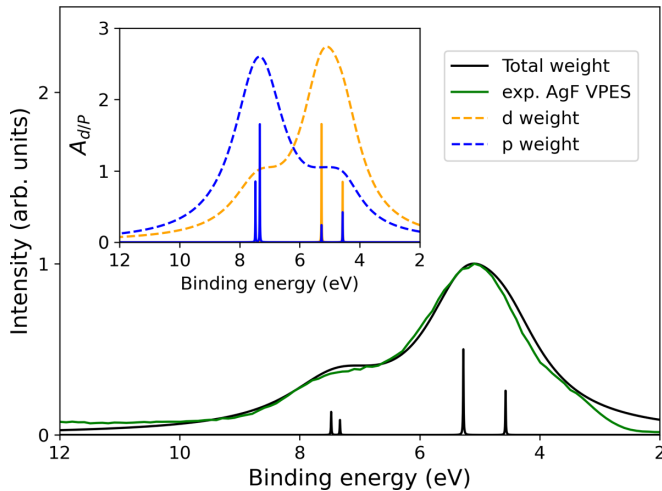
FIG. 2. Comparison between the valence XPS experimental spectrum (green) and cluster model calculation (black) of the AgF compound. In the computations we fixed hybridization matrix elements as explained in the text yielding $T_{pd}^{x^2-y^2} = 1.38$ eV and $T_{pp} = 0.29$ eV. The best fit to the experiment was found with $\Delta_{pd} = 1.2$ eV. We show the computation with a very narrow broadening to resolve the position of individual excitations and intensities and with a phenomenological Lorentzian broadening growing linearly in energy ($\eta = 0.97$ eV $+0.14\omega$) to fit of the experiment. The inset shows the computed silver-d (orange) and fluorine-P (blue) spectral functions.
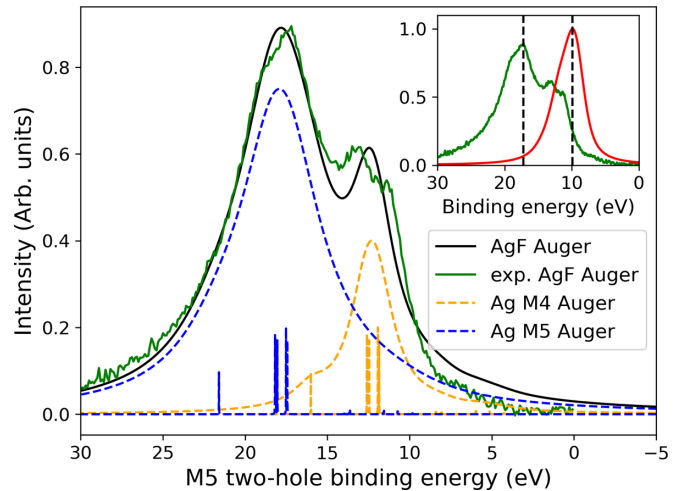

FIG. 3. Comparison between Auger experimental spectrum (green) and Auger cluster model calculation spectrum (black) of the AgF compound. The black curve is given by the summation of the $M4$ and $M5$ singlet spectra. The two main structures are due to the SO splitting in the Ag $3d$ subshell (see Appendix B 1). The broadening of the $M4$ component is $\eta = 2.6$ eV and the one of the $M5$ component is $\eta = 5.6$ eV. The fit between experimental and theoretical data fixes $\overline{U}_{dd} = 6.0$ eV. Other cluster parameters are the same as in Fig. 2. In the inset, the self-convolutions of the experimental valence band XPS spectrum (red) and the experimental Auger spectrum (green) are shown. The energy splitting (dashed black vertical lines) between those two peaks is equal to 7.3 eV and represents a rough estimate of $U(^1G)$ in the Ag $4d$ subshell.

which is well suited to probe two-hole interactions in silver [16,31] in a fluorine environment, just as Ag_2O and Cu_2O were used for the same purpose in an oxygen environment [6,29].

The green line in Fig. 3 shows the MNN Auger spectra of AgF which is better resolved than previous measurements [32]. In this process, a core hole is created in the $3d$ shell which is filled by a $4d$ electron with the simultaneous ejection of a second $4d$ electron resulting in a formally d^8 final state, the energy of which is determined by the hole-hole Coulomb repulsion. Indeed, if the two holes were not correlated, one should find a spectral function given by the convolution of the one-hole spectral function of Fig. 2. Instead, for correlated holes one finds a significant shift [16,31,33,34] which is approximately given by $U(^1G)$ on silver. This is shown in the inset of Fig. 3 which compares the convoluted one-particle spectra (red line) and the Auger spectra with the binding energy computed assuming an $M5$ initial state (see Appendix B1). The distance between the peaks is 7.3 eV, which provides a first estimate of $U(^1G)$.

A more accurate value of the silver on-site repulsion can be obtained with the cluster computation, which is shown in the main panel of Fig. 3 and compared with the experimental result. From the fit, we find $\overline{U}_{dd} = 6.0$ eV. This corresponds to $U(^1G) = 7.16$ eV which is close to the above estimate and can be compared with $U(^1G) = 5.8$ eV for the closed-shell *oxide* Ag_2O found by Tjeng *et al.* [6] using the same technique. The intraorbital repulsion in AgF amounts to $U_{4d} = 7.7$ eV.

In both silver compounds the Hubbard repulsion is much smaller than for a free Ag^{2+} ion [$U(^1G) = 14.8$ eV] due to the strong screening by the environment [24–26,35,36]. Furthermore, the different on-site repulsion between AgF and Ag_2O

can be attributed to differences in that screening. Indeed, F^- is roughly a factor of 2 less polarizable [24] than O^{2-} and the Ag-F distance is 2.468 Å, larger than the Ag-O bond length of 2.05 Å. Since the decrease in the on-site interaction is proportional to the polarizability of the environment and decreases with the metal-ligand distance to the fourth power, we conclude that both effects lead to less screening (larger repulsion) on the fluoride. On the other hand, Ag_2O is linearly coordinated with 2 O^{2-} while AgF is octahedrally coordinated with 6 F^-, which may partially compensate this effect. Clearly, the reduced screening prevails, so the on-site Coulomb repulsion is significantly larger in AgF than in Ag_2O. The $U(^1G)$ value in AgF is smaller than $U(^1G) = 9.2$ eV, the value found [29] in closed-shell Cu_2O, but it is still sizable.

C. Valence band photoemission of AgF_2

Having established the strength of onsite repulsion in AgF we now turn to the valence band photoemission spectra of AgF_2. As for CuO one expects a "one-hole" ground state consisting of a mixture of d^9 and $d^{10}\underline{L}$ configurations.

The experimental spectrum is shown in green in Fig. 4. The spectrum has some similarity with the AgF spectra, except that the band is broader and the high-energy shoulder is less marked. XPS is a very surface sensitive technique. AgF_2 grains may have lost F at the surface, so it is possible that the spectrum corresponds to $AgF_{2-\delta}$ with some unknown δ. To address this issue, we show in Appendix B 2 core-hole spectra of the various compounds. The $3d$ chemical shifts point to
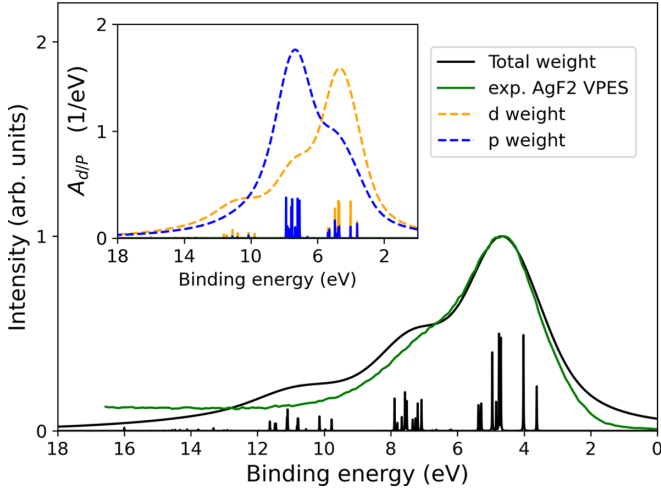
FIG. 4. Valence band XPS spectra of AgF$_2$. The green line is the experimental result and the black line is the result of the cluster computation with the crystal field parameters of Table I and $\overline{U}_{dd} = 5.5$ eV ($U_{4d} = 7.2$ eV), $\overline{U}_{pp} = 6$ eV, $U_{pd} = 1$ eV, $\Delta_{pd} = 4$ eV, and $T_{pd} = 2.76$ eV. We used a Lorentzian broadening $\eta = 0.83 + 0.17\,\omega$ eV and convolution with a Gaussian of FWHM = 1.0 eV (green line). We also show the theory with a very small broadening to show the energy of individual states in the cluster (black line). The inset shows the computed character of the spectra: $A_d(\omega)$ (orange dashed line) and $A_P(\omega)$ (blue dashed line). For the theory, the zero of the energy is set at the additional chemical potential. For the experiment, the spectrum was shifted in energy to align its main features to the cluster computation.

a higher oxidation state in the nominal AgF$_2$ sample than in AgF. However, satellites which could confirm the d^9 character of the ground state were not seen. In the following, we assume a one-hole ground state and come back to this problem in the Conclusions section.

For an N-electron system with ground-state energy $E_0(N)$, photoemission probes the many-body states with $N-1$ electrons which in our case is the Hilbert space spanned by the d^8, $d^9\underline{L}$, and $d^{10}\underline{L}^2$ configurations. We will discuss two possible theoretical scenarios which are plausible with the present data: one using the DFT crystal fields yielding a weakly bound Zhang-Rice (ZR) state [37,38] and another using an *ad hoc* set of crystal fields yielding a strongly bound ZR state.

1. Weakly bound Zhang-Rice state scenario

The black line in Fig. 4 is the cluster computation with the DFT crystal field energies from Table I and parameters indicated in the caption. In the inset, we show the d and P spectral functions. The theory shows a main peak and a somewhat more intense shoulder than in the experiment, and a secondary shoulder which is either not visible in the experiment or hidden by the background.

As will be shown below, the narrow theoretical peak (black line) with smaller binding energy (3.6 eV) corresponds to the ZR state [37,38]. This is the first ionization state of the system, therefore its binding energy coincides with the chemical potential to remove one electron, defined as $\mu^- \equiv E_0(N-1) - E_0(N)$. We have used the freedom to choose the zero of the one-particle energy levels in our computations
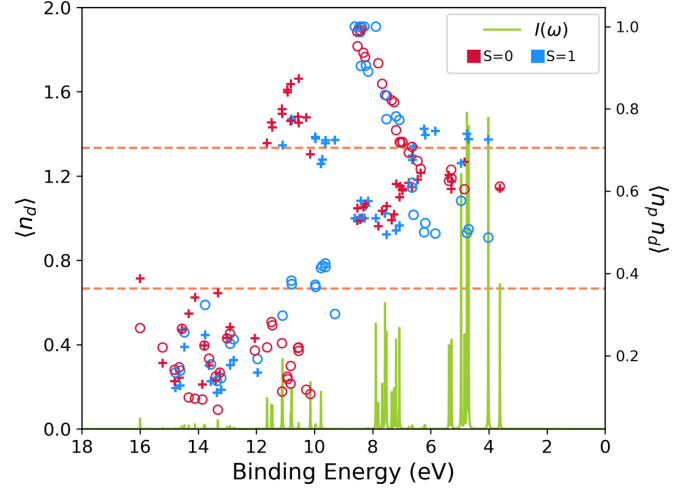

FIG. 5. The crosses are the hole occupancy of the d states (left scale) while the circles are the interatomic charge correlator (right scale) in the possible final states of the photoemission process. The colors of the symbols encode the singlet (red) or triplet (blue) character of the two-hole state. Parameters and binding energies are defined as in Fig. 4. At the bottom, we show the valence band spectrum in green to facilitate identification of the states. The horizontal lines are guide to the eyes separating large, small, and intermediate values of the expectation values.

in such a way that the addition of chemical potential $\mu^+ \equiv E_0(N+1) - E_0(N)$ coincides with zero binding energy. In this way, the ZR binding energy yields also the charge gap of the system, $E_{\text{gap}} \equiv \mu^+ - \mu^- = 3.6$ eV in Fig. 4. In Appendix B we report the experimental binding energies with a standard reference for charging effects and compare with literature values.

In order to characterize the excited states, Fig. 5 shows $\langle n_d \rangle$, the hole occupancy in d orbitals, and the correlator $\langle n_d n_p \rangle$ of all possible two-hole states in the cluster, as a function of their binding energy in the photoemission spectra. Here we defined $n_d \equiv \sum_v d_v^\dagger d_v$ and $n_p \equiv \sum_v P_v^\dagger P_v$. n_d projects on the subspace spanned by d^8 and $d^9\underline{L}$ configurations while $n_d n_p$ projects on the $d^9\underline{L}$ subspace. Clearly, these two expectation values take integer values in these subspaces:

$$\langle n_d \rangle = 2, \quad \langle n_d n_p \rangle = 0, \quad (d^8),$$
$$\langle n_d \rangle = 1, \quad \langle n_d n_p \rangle = 1, \quad (d^9\underline{L}),$$
$$\langle n_d \rangle = 0, \quad \langle n_d n_p \rangle = 0, \quad (d^{10}\underline{L}^2).$$

Therefore, for general states, the expectation values and completeness characterize the probability of the three possible configurations. For example, a state with $\langle n_d \rangle \approx 1$ may indicate a $d^9\underline{L}$ state or an equally mixed d^8 and $d^{10}\underline{L}^2$ configuration. The $\langle n_d n_p \rangle$ correlator allows distinguishing among these two possibilities or intermediate situations. We use red and blue in Fig. 5 to distinguish singlet and triplet final states, respectively. We also show the spectra as narrow peaks as a reference.

The main peak in the XPS experiment (see Fig. 4) can be attributed to states with $\langle n_d \rangle \approx 1$ and also intermediate interatomic charge correlations, indicating a mixed character (states between 3 and 6 eV). The main shoulder (states
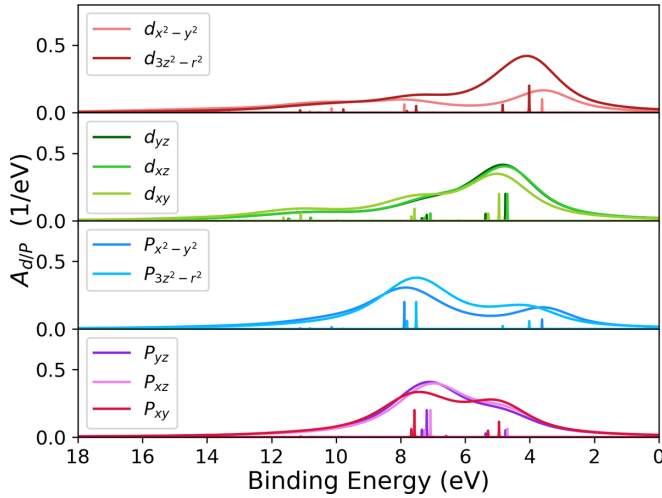
FIG. 6. One particle spectral function projected on the different orbital symmetries of the cluster for the same parameters as Fig. 4.
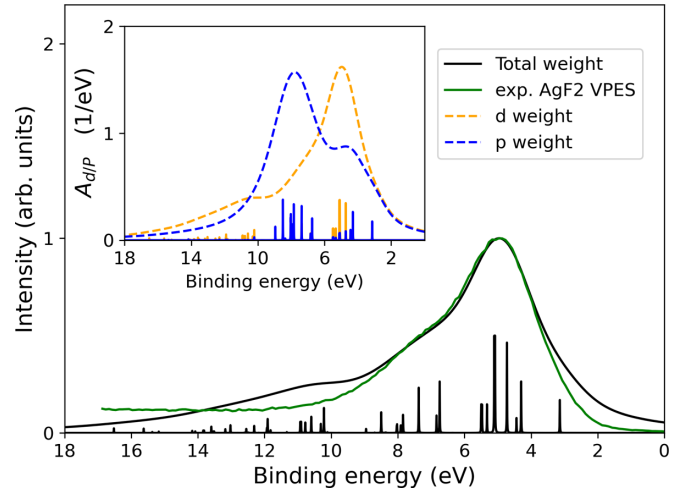

FIG. 7. Same as Fig. 4 for the *ad hoc* crystal field parameters of the strongly bound ZR scenario. Other parameters are $\overline{U}_{dd} = 6.5$ eV corresponding to $U_{4d} = 8.2$ eV, $\overline{U}_{pp} = 6.0$ eV, $\Delta_{pd} = 3.5$ eV, and $U_{pd} = 1.5$ eV. The theoretical curve (black) is presented with a phenomenological broadening with a Lorentzian parameter varying linearly with energy as $\eta = 0.45$ eV $+ 0.30\,\omega$ (green line) and with a very small broadening to show the energy of individual states in the cluster (black line). The inset shows the computed character of the spectra: $A_d(\omega)$ (orange dashed line) and $A_P(\omega)$ (blue dashed line).

between 6 and 8 eV) is characterized by final states with large interatomic charge correlations, indicating a prevalent $d^9\underline{L}$ character. The secondary shoulder (states with energy between 9 and 12 eV) is due to states with large $\langle n_d \rangle$ and small interatomic charge correlations, which indicates a prevalent d^8 character. Above 12 eV states with small d spectral weight appear, the small $\langle n_d \rangle$ of which indicates a $d^{10}\underline{L}^2$ character.

Figure 6 shows the orbital resolved spectral function. Combining with Fig. 5 we see that the leading narrow peak corresponds to a singlet final state with orbitals with dominant $x^2 - y^2$ character and a sizable weight in the $d^9\underline{L}$ configuration. As anticipated, we can identify this state with the ZR singlet of cuprates [37,38].

One can see that the energy gap of the singlet state with respect to the triplet, i.e., the difference of their binding energies, is quite small indicating that it competes with a predominantly d^8 high-spin state [39] with the second hole in the d_{z^2} orbital. The present parameter set has larger Δ and smaller U_{4d} with respect to the parameter set to be analyzed in what follows (and with respect to cuprates). The small stability of the ZR singlet is in accord with the results of Ref. [37] where the stability of the singlet decreases with $\Delta - U_{4d}$. In particular, the present weakly bound ZR scenario is similar to a recent proposal for nickelates [40]. Note that the d^8 high-spin state is the Hund-rule ground state in a scenario where the charge gap is of the Mott type in the Zannen-Sawatzky-Allen (ZSA) classification scheme [37]. Thus the present scenario is of the charge-transfer type but close to the Mott regime.

In general the relative weight of the shoulder with respect to the main peak decreases with increasing $\overline{U}_{pp}$, thus the fitting improves for $\overline{U}_{pp} = 10$ eV. However, the effect is rather small as $d^{10}\underline{L}^2$ configurations do not appear directly in the spectrum; as a consequence this method lacks sensitivity to determine $\overline{U}_{pp}$. One can obtain a similar result increasing Δ_{pd} beyond 4 eV. These values, however, would be in strong contradiction to the RIXS and optical experiments of Ref. [14].

2. Strongly bound Zhang-Rice state scenario

To illustrate the sensitivity of U_{4d} and Δ_{pd} to the choice of diagonal energies representing fluorine states, we show

the spectra with an *ad hoc* set of crystal fields. Namely, we replace the values in Table I by $e_P^\nu = 1.5, -1.5, -1.5, 0.75$, and 0.75 (all values in eV) for $\nu = z^2, x^2 - y^2, xy, xz$, and yz, respectively. Furthermore, following Refs. [6,21,29] we neglect the crystal field on silver ($\epsilon_d^\nu = 0$). As shown in Fig. 7, in this case, we find that a good fit can be obtained with $U_{4d} = 8.2$ eV and $\Delta_{pd} = 3.5$ eV. The fit of the main shoulder is improved, but there is still substantial spectral weight in the second shoulder which is not seen in the experiment.

Now the ZR singlet is well separated from the rest of the spectra, justifying the subsection title. From Figs. 8 and 9 one sees that the P character of the ZR state is reinforced with respect to the previous case, increasing the resemblance to cuprates.

Since the present parameter set has larger U_{4d} and smaller Δ_{pd}, the highest-energy state in the removal spectra near 16.5 eV now has a significant component with the two holes in the $x^2 - y^2$ orbital (see Figs. 8 and 9) instead of being dominated by $d^{10}\underline{L}^2$ configurations as in the weakly bound ZR case presented in Sec. IV C 1. Unfortunately also, this upper Hubbard band structure is not visible in the experiment, hampering a direct determination of U_{4d}.

In the previous case of small crystal field parameters, the spectra of the different symmetries (except $x^2 - y^2$) resemble each other (see Fig. 6) which leads to a clustering of peaks in the photoemission spectra with similar character of final states (see Fig. 5). For the larger crystal fields considered here, the peaks acquire a more heterogeneous character, as witnessed by the expectation values in Fig. 8. The d_{xy} spectral weight in Fig. 9 is shifted to smaller energies and differs from the other symmetries, which is enough to substantially increase the agreement between theory and experiment.
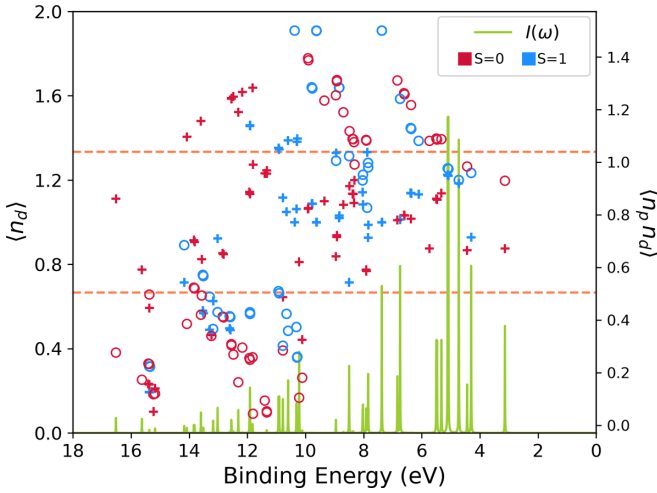
FIG. 8. The crosses are the hole occupancy of the d states (left scale) while the circles are the interatomic charge correlator (right scale) in the possible final states of the photoemission process. The colors of the symbols encode the singlet (red) or triplet (blue) character of the two-hole state. Parameters and binding energies are defined as in Fig. 7. At the bottom, we show the valence band spectrum in green to facilitate identification of the states.

D. dd excitations and gap

A recent RIXS study [14] has found a set of dd transitions laying between 1.4 and 2.7 eV, very similar to the ones observed previously in cuprates. To explain the dd transitions and a parallel optical study, similar cluster computations were performed but using a model that neglected U_{pp} and U_{pd}. Fitting the optical and the RIXS spectra required using different parameters for optics and RIXS. A 20% increase of T_{pd} with respect to the DFT value and a quite small value of the charge-transfer parameter, $\Delta = 1.29$ eV, were required to match the dd transitions. On the other hand, optical excitations required a much larger value of the charge-transfer parameter, $\Delta = 2.8$ eV. It was argued that the difference could be explained, taking into account $U_{pd} \sim 1.5$ eV in an effective
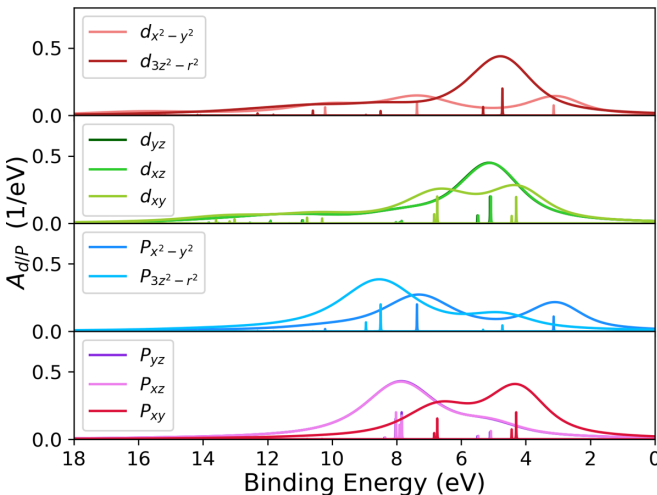

FIG. 9. One particle spectral function projected on the different orbital symmetries of the cluster for the same parameters of Fig. 7.

TABLE II. Energy of dd transitions $x^2 - y^2 \rightarrow \nu$ from Refs. [21] (theory, three parameter sets) and [14,41] (experiment) and the present computations in the weakly bound (WB) and strongly bound (SB) ZR scenario. The first column labels the transitions by the final state ν. Since single crystal studies are not available, the dd transitions of AgF$_2$ have not yet been assigned to specific symmetries. We report the approximate location of the lower and higher energy feature, which have been tentatively assigned to specific symmetries with the aid of the DFT computations in Ref. [14]. For the experimental gap, we report the peak in the optical conductivity from Refs. [14,42].

| | La$_2$CuO$_4$ | | | | AgF$_2$ Theory | | |
| | Theory | | | Expt. | This paper | | Expt. |
Ref.	[21]	[21]	[21]	[41]	WB ZR	SB ZR	[14]
z^2	1.42	1.28	1.20	1.70	0.96	1.51	1.5
xy	1.53	1.40	1.35	1.80	1.54	1.25	
xz	1.60	1.51	1.56	2.12	1.48	1.68	2.4
yz	1.60	1.51	1.56	2.12	1.50	1.70	
E_{gap}	1.2	1.8	2.4	2.2	3.6	3.1	3.4
n_d	0.60	0.66	0.72		0.80	0.67	

manner. Unfortunately, the large number of free parameters does not allow for a systematic fit of U_{pd}, hence we fixed it to a value close to the one in Ref. [14].

From Table II we see that the weakly bound ZR scenario underestimates the value of low-energy dd transitions while the strongly bound ZR scenario performs slightly better but underestimates the high-energy part. A similar problem occurs with the cluster computations of Ref. [21] shown in the same table. The agreement can be improved taking into account interactions beyond the cluster, as done in Ref. [19]. For example, within the cluster the one-hole state is a mixture of d^9 and $d^{10}\underline{L}$ configurations with $x^2 - y^2$ symmetry. Taking into account the interaction of these one-hole states beyond the cluster gives rise to the superexchange magnetic interaction, which lowers the energy of the state by a quantity of the order of J per Ag ion. This lowering will be nearly zero in the excited states, since they are much more localized due to a smaller T_{pd}^ν. Therefore, one should increase the excitation energy by a quantity of order [8] $J = 0.07$ eV in AgF$_2$ and 0.1 eV in cuprates. An accurate determination of dd transitions of cuprates in quantum chemistry computations [19,20] required the consideration of a large number of additional atoms with respect to what we considered here. So part of the disagreement found can be just a limitation of the present cluster computations and not attributed to the parameters used.

The optical experiments of Ref. [14] in powder samples did not allow determining the gap unambiguously. A peak value was reported at 3.4 eV but the onset of the nonexcitonic charge-transfer absorption was estimated around 2.2 eV. Such value, however, depends on assumptions about the powder average and the role of disorder on the measurements and should be taken with some skepticism. The fundamental gap for the parameters studied is shown in Table II. While the gap for the weakly bound ZR scenario is slightly too large, the

uncertainties on the optical data do not allow excluding this scenario on the basis of this comparison alone.

V. COMPARISON WITH THE HUBBARD U INTERACTION IN THE DFT+U METHOD

Until now we have obtained estimates of the intraorbital Hubbard U_{4d} interaction in fluorides from spectroscopic experiments. Since the work of Anisimov *et al.* [43] it is customary in DFT computations of correlated systems to incorporate a Hubbard U parameter (hereafter U^*) to cure some deficiencies of the particular functional in use. It is often assumed that the parameter of the DFT method should correspond to a physical repulsion such as $U^* = U_{4d}$. However, this equivalence is far from obvious. Indeed, for the exact functional, no correction is needed [44] and $U^* = 0$. Thus, it is clear that U^* depends on the approximate functional in use, while U_{4d} is an observable spectroscopic quantity depending only on the material.

Setting $T^\nu_{pd} = 0$ and taking the d shell as an example, one can quite generally define

$$U_{4d} = E(d^{10}) + E(^1A_{1g}, d^8) - 2E(d^9), \tag{2}$$

where the notation emphasizes that the d^8 state should be a singlet with both holes on the same orbital. Assuming DFT provides accurate total energies at integer occupations, it is reasonable to estimate the physical U_{4d} using the above formula in a DFT computation in which the d shell occupancy is constrained at $n = 8, 9, 10$ and the hybridization is suppressed. Indeed, this kind of computation was done even before the DFT+U methodology was proposed [45,46].

The values of $E(d^n)$ at three points ($n = 8, 9, 10$) are enough to define a parabola. For common local or semilocal functionals, such as local-density approximation or generalized gradient approximation, the energy as a function of n, taken now as a *continuous variable*, is expected to follow an approximate parabolic behavior. Instead, the energy computed with the exact functional is known to be piecewise linear, coinciding with the parabolic behavior only at integer values of n [44]. Cococcioni and de Gironcoli (CDG) proposed [44] to introduce U^* in such a way that the piecewise linear behavior is restored in the approximate DFT+U functional. It is easy to see that if the energy computed with a given functional is a parabola *for all real n* in the interval $8 \leqslant n \leqslant 10$ then the CDG correction coincides also with the DFT estimate of the spectroscopic interaction using Eq. (2). Therefore, we can take $U^* = U_{4d}$ where the left-hand side is the Hubbard interaction in the DFT+U method while the right-hand side should be understood as the DFT approximation to the spectroscopic interaction using Eq. (2). This, of course, does not hold for an exact functional or for any functional which does not yield a perfect parabola in the full interval $8 \leqslant n \leqslant 10$.

We have computed the Hubbard U parameters both for Ag and F in AgF$_2$, using the linear response approach of CDG as implemented in the VASP software package [47,48]. The Monkhorst-Pack sampling of the k mesh was $6 \times 6 \times 7$, and the energy cutoff for the plane-wave basis was set as 520 eV. The PBEsol implementation of the exchange-correlation functional was used.

TABLE III. Comparison of parameters between AgF$_2$ (current paper) and CuO (from Ref. [57]). All values are in eV. U_{4d}/U_{3d} is the intraorbital repulsion $U(^1A_{1g})$.

	AgF$_2$	CuO
$T_{pd}^{x^2-y^2}$	2.76	2.5
T_{pp}	0.11[a]	1.0
Δ	3.5–4.1	2.95
U_{4d}/U_{3d}	7.2–8.2	8.8
U_{pp}	6.0	
U_{pd}	1–1.5	<1[b]
E_{gap}	3.4	1.8
n_d	0.67–0.80	0.66

[a]For comparison for AgF$_2$ we defined an effective $T_{pp} = [e_P(xz) + e_P(yz)]/2 - e_P(x^2 - y^2)$ with the crystal field parameters of Table I.
[b]E_{gap} and n_d are from Ref. [21] which did not include this parameter.

We obtained $U^*(\text{Ag}) = 5.31$ eV and $U^*(\text{F}) = 11.18$ eV. The value for Ag is smaller than $U_{4d} = 7$–8 eV obtained from the spectroscopic data, while the value for F is probably larger than the physical one. These disagreements are not uncommon. For example, for NiO Ref. [44] finds $U^*(\text{Ni}) = 4.6$ eV, while the spectroscopic value [49] for antiparallel spin is $U_{3d} = 10$ eV. This difference may be due to inaccuracies of the DFT approximate energies at integer values (a problem that is simply not addressed by the CDG method) or to a nonparabolic behavior of the energy in between. For closed-shell ions (such as nominal F$^-$) overestimation of the Hubbard U by the linear response method is common [50]. A resolution of these issues is certainly very interesting and deserves further theoretical research, but goes beyond our present scope. Even if the physical and the corrective U^* do not coincide, consistency of the method requires that the above value of $U^*(\text{Ag})$ is used in DFT+U computations with the PBEsol functional.

VI. DISCUSSION AND CONCLUSIONS

We have presented a high-energy spectroscopy study complemented with cluster computations to determine the degree of correlations in silver fluorides and their similarities and/or differences with cuprates.

DFT computations predict very similar $p - d$ hopping matrix elements in the two compounds (see Table III). Many important differences in electronic parameters can be traced back to the different size of the orbitals: Ag^{2+} is larger than Cu^{2+} while F$^-$ is smaller than O^{2-}. The ion polarizability scales with the ionic volume, while the on-site Coulomb repulsion decreases with the size. For the more localized fluorine p orbitals, we expect larger U_{pp} and smaller $p - p$ hybridization and ligand polarizability in the silver fluoride. For d orbitals the roles are interchanged, and we expect smaller bare on-site interaction which is compensated by smaller screening by the ligands.

Our computations for closed-shell AgF are in good agreement with the experiment. Using valence band photoemission and Auger spectroscopy, we were able to estimate the Hubbard Coulomb repulsion among two holes on the same orbital to be $U_{4d} = 7.7$ eV. As expected, this is smaller than the same

quantity in cuprates which is partially compensated by the screening effect.

For valence band photoemission of AgF_2, the situation is more complicated. The spectrum shows a peak and a shoulder. This resembles the spectra observed in cuprates which, however, show also high binding energy satellites at a distance of 7–8 eV from the main peak. Unfortunately, such satellites— which in cuprates are related to d^8 states—are not seen here, hampering a direct determination of U_{4d} in AgF_2. Due to the large number of parameters and the small number of observed features, a systematic fit was not possible. Thus, we considered two possible scenarios, a weakly bound and a strongly bound ZR singlet, that allowed us to constrain the parameters U_{4d} and Δ_{pd} and provide a reasonable range of possible values. Table III compares the parameters found for AgF_2 and CuO. In both considered scenarios, the charge-transfer energy is somewhat larger and the Coulomb repulsion is smaller than in cuprates. However, in both scenarios the Coulomb repulsion dominates, and the material can be classified as a charge-transfer insulator according to the ZSA scheme.

The value found for $\Delta_{pd} = 1.2$ eV in AgF is considerably smaller than in AgF_2. In both materials, we defined Δ_{pd} as the energy cost of the ionic transition $d^9 \rightarrow d^{10}\underline{L}$. The difference in Δ_{pd} can be understood considering the ionic potential. The energy of the hole in the silver site is decreased the shorter the distance to the negatively charged fluorines. In contrast, the energy of the hole on the ligand increases when shortening the distance with the positively charged silver. Thus the increase of the charge-transfer energy can be attributed in part to elementary electrostatic considerations and to the decrease of the Ag-F distance when going from AgF (2.47 Å) [51] to AgF_2 (2.07 Å) [52].

The weakly bound scenario used to explain the photoemission experiment in AgF_2 predicts a small energy difference between a high-spin d^8 state and a low-spin ZR singlet. It is worth mentioning that in DFT doped holes on AgF_2 planes form both low-spin [53] and high-spin [54] solutions depending on details such as the local strain and the environment. This sensitivity to details is compatible with a weakly bound ZR scenario. Unfortunately, these computations neglect important correlation effects and should not be trusted to determine the first ionization state of the insulator for reasons similar to the ones discussed in Sec. V. Overall, the strongly bound ZR scenario gives a better match of the spectra and of dd transitions, but the improvement is marginal with respect to the uncertainties involved, so we cannot narrow more the range of parameters from what is shown in Table III.

The puzzling absence of d^8 satellites in the valence band photoemission spectrum can be due to overlap with other bands which strongly broaden these states or off-stoichiometry at the surface. In cuprates it has been demonstrated that the photoemission intensity of these features can be strongly enhanced by tuning the photon energy to be resonant with the core $3p$ threshold excitation [55] (74 eV) and the core $2p$ threshold [56] (931 eV). It would be highly desirable to perform similar experiments in AgF_2. A good candidate could be the $4p$ edge (56 eV) which shows [6] a weak resonance in Ag_2O.

The photon energy used in this paper (Al-Kα) makes the spectra dominated by the d weight. It would be very interesting to repeat the experiment with other light sources which are sensitive to the p spectral weight, like He I and He II lines [σ(F $2p$) and σ(Ag $4d$) = 0.84 and 0.34, respectively]. This would allow identifying the structures predicted in the inset of Figs. 4 and 7. If the strongly bound ZR scenario is correct, a distinctive feature associated with this state should appear at low binding energy due to the high fluorine p character of the removal states. Similar features are well known in cuprates [29]. This will unambiguously identify the character of the first removal state, which is also fundamental to determine the nature of possible hole doping that can be achieved in this compound.

In general, the fit of the photoemission data in AgF_2 requires a larger charge-transfer energy than the one suggested by the analysis of dd transitions in AgF_2; on the other hand, analysis of optics data yields a similar value to the one found here. RIXS analysis of single crystal data would be highly desirable to identify the symmetry of the different dd transitions and can serve to better constrain the crystal field splittings.

The value of $U_{4d} = 7.7$ eV found for AgF confirms that silver fluorides have a large Coulomb repulsion. Also, AgF has a small value of the charge-transfer gap which suggests that AgF_2 should also be a quite covalent material. Indeed, analyzing the photoemission spectra of AgF_2, we arrived to the conclusion that it is a correlated insulator of charge-transfer type just as the insulating parent compounds of high-T_c superconductors. It appears to have a degree of covalency similar to cuprates and a somewhat smaller Coulomb repulsion on the transition metal ion. The repulsion on the ligand is expected to be larger than in cuprates. This, however, has a minor role in the low-energy physics, as the probability of two holes to be on the same ligand is anyway small.

Unfortunately, we cannot exclude that fluorine loss on the surface has affected the spectra of AgF_2 making it resemble that of AgF (or electron doped AgF_2). Core-level spectroscopy discussed in Appendix B 2, although in accord with previous literature, does not give an unambiguous answer to this problem. In the case of AgF_2, such possible contamination of the spectra may affect the parameters derived which, thus, should be taken as tentative until the experimental spectra can be confirmed in more controlled surfaces. A step forward in this direction could come from single crystals, particularly at low temperature, to minimize the decomposition of the surface. Efforts for their synthesis using an electrochemistry method [58] are underway.

The similarity with cuprates suggests that AgF_2 can become the corner stone of a new family of high-T_c superconductors. However, due to the strong buckling, doping the bulk material may lead to strong polaronic effects [53]. A more fruitful approach would be to grow two-dimensional AgF_2 in an appropriate substrate with doping from donor [54] layers or gating. It has been predicted [9] that this may lead to d-wave high-T_c superconductivity of the order of 200 K.

APPENDIX A: TREATMENT OF COULOMB REPULSION ON FLUORINE

Because p orbitals in fluorine are more localized than in oxygen, intraorbital repulsion may be more relevant. Therefore, we treat it explicitly rather than in mean field as customarily done in cuprates.

To reduce the Hilbert space in the cluster computations, we constructed symmetry adapted P orbitals which are linear combinations of p orbitals with strong overlap with the d orbitals. This requires us to write the atomic Coulomb operator on fluorine in the basis of P orbitals. This defines the matrix elements U^{PP} appearing in Eq. (1). In the following, we present the derivation of this matrix.

For simplicity, we take into account only the monopole part of the interaction on each fluorine atom. The Coulomb operator reads

$$H_{U_{pp}} = \frac{U_{pp}}{2} \sum_{r\alpha\alpha'\sigma\sigma'} \bar{p}^\dagger_{r\alpha\sigma} \bar{p}^\dagger_{r\alpha'\sigma'} \bar{p}_{r\alpha'\sigma'} \bar{p}_{r\alpha\sigma}$$

with $\bar{p}^\dagger_{r\alpha\sigma}$ creating an *electron* in fluorine r with orbital and spin quantum number $\alpha\sigma$. r runs over the $N_F = 6$ fluorine sites around the central Ag and $\alpha = x, y, z$.

The symmetry adapted orbitals are defined by

$$\bar{P}^\dagger_{m\sigma} = \sum_{r\alpha} \phi_{m,r\alpha} \bar{p}^\dagger_{r\alpha\sigma}$$

with $\phi_{m,r\alpha}$ a 18×18 unitary matrix. The inverse transform reads

$$\bar{p}^\dagger_{r\alpha\sigma} = \sum_{r\alpha} \phi^*_{r\alpha,m} \bar{P}^\dagger_{m\sigma}.$$

After this projection, the interaction reads

$$H_{U_{pp}} = \frac{U_{pp}}{2} \sum_{m_1 m_2 m_3 m_4 \sigma\sigma'} M^{m_1 m_2}_{m_3 m_4} \bar{P}^\dagger_{m_1\sigma} \bar{P}^\dagger_{m_3\sigma'} \bar{P}_{m_4\sigma'} \bar{P}_{m_2\sigma}$$

with

$$M^{m_1 m_2}_{m_3 m_4} = \sum_{r\alpha\alpha'} \phi^*_{r\alpha,m_1} \phi^*_{r\alpha',m_3} \phi_{r\alpha',m_4} \phi_{r\alpha,m_2}.$$

M is a symmetric $18^2 \times 18^2$ matrix with rows and columns labeled by the pairs $m_1 m_2$ and $m_3 m_4$ with $m_i = 1, \ldots, 3N_F$. In the Hilbert space of interest only a small portion of this matrix is needed, as discussed below.

Transforming to the hole formalism of the main text ($\bar{P}^\dagger_{m\sigma} \rightarrow P_{m\sigma}$) one obtains

$$H_{U_{pp}} = E_{cs} + \sum_{m\sigma} \epsilon^m_{U_{PP}} P^\dagger_{m\sigma} P_{m\sigma}$$

$$+ \frac{U_{pp}}{2} \sum_{m_1 m_2 m_3 m_4 \sigma\sigma'} M^{m_1 m_2}_{m_3 m_4} P^\dagger_{m_4\sigma'} P^\dagger_{m_2\sigma'} P_{m_1\sigma'} P_{m_3\sigma} \quad \text{(A1)}$$

with the energy of the closed shell given by a direct and exchange contribution which can be put in the familiar form

$$E_{cs} = U_{pp} \sum_{m_1 m_2} 2\left(M^{m_1 m_1}_{m_2 m_2} - M^{m_1 m_2}_{m_2 m_1}\right) = U_{pp} N_F \frac{N_s(N_s - 1)}{2}$$

with $N_s = 6$, the number of spin orbitals in a p shell.

After normal ordering one obtains single-particle contributions defined by

$$\epsilon^m_{U_{pp}} = -U_{pp} \sum_{m'} \left(2M^{m'm'}_{mm} - M^{m'm}_{mm'}\right) = -U_{pp}(N_s - 1).$$

This clearly represents the interaction of the removed electron with the other electrons in a given fluorine. Since this is independent of m, it can be incorporated in the definition of Δ. Following Ref. [14], we can now separate the symmetry adapted orbitals into five orbitals with significant mixing with the central Ag and the rest. The former transform approximately as d orbitals and are labeled accordingly as $m = z^2$, $x^2 - y^2$, xy, xz, and yz. Neglecting irrelevant terms, the final form of the interaction reads as Eq. (1) where now the sum is restricted to the symmetry adapted orbitals with $\nu_i \rightarrow m_i\sigma_i$ and

$$U^{(PP)}(m_1\sigma_1, m_2\sigma_2, m_3\sigma_3, m_4\sigma_4) = \frac{U_{pp}}{2} M^{m_4 m_1}_{m_2 m_3} \delta_{\sigma_1\sigma_4} \delta_{\sigma_2\sigma_3}.$$

APPENDIX B: BINDING ENERGIES

Here, we present core-hole spectra of the materials studied. On one hand, this is useful to define the two-hole binding energies in the Auger process. Furthermore, core-hole spectra may give information on the oxidation state of the region of the sample under examination.

In order to compensate for charging effects in insulating samples, all the binding energies were corrected aligning the C $1s$ peaks from contaminants with the C $1s$ peak of a reference metallic Ag sample.

1. Two-hole binding energies in the Auger process

In a two-step description of the Auger process, the initial state consists of a core-hole state, followed by the decay of a valence electron and the emission of a second valence electron, ending in a state with two valence holes. For AgF the initial core hole can be in a $3d_{3/2}$ ($M4$) or a $3d_{5/2}$ state ($M5$) which are separated by the spin-orbit splitting $\Delta_{\text{SO}} = 6.0$ eV as revealed by the core-level spectra shown in Fig. 10. Focusing on the case in which the initial core hole is in the $M5$ state, the two-hole binding energy corresponding to a two-particle excitation ν is given by $E_b(\nu) = E(N - 2, \nu) - E(N, 0) = E(N - 1, M5) - E(N, 0) - KE$ where the kinetic energy of the photoejected electron is $KE = E(N - 1, M5) - E(N - 2, \nu)$. Here, $E(N, 0)$ is the N-particle ground state. In Fig. 3
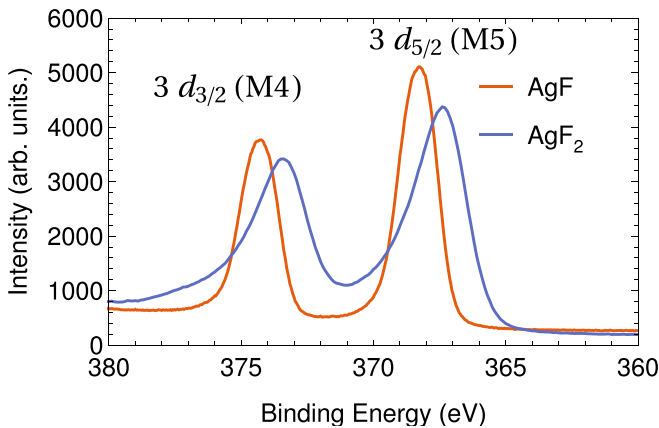
FIG. 10. The measured *3d* core-hole spectra of AgF and AgF_2. The splitting between the $M4$ and $M5$ states is due to spin-orbit coupling and amounts to $\Delta_{SO} = 6.0$ eV for AgF.

FIG. 11. The measured *3p* core-hole spectra of AgF and AgF_2.

since we choose to plot the spectrum in terms of the $M5$ binding energy, the spectrum corresponding to the $M4$ initial state appears at smaller binding energy and shifted by the spin-orbit coupling Δ_{SO}.

2. Oxidation state

Chemical shifts provide information on the oxidation states. Usually the binding energy increases with the oxidation state but compounds of silver are anomalous in that they show the opposite effect [17,32,59–61].

For AgF, the binding energy of the $3d_{5/2}$ state from Fig. 10 is 368.3 eV. This is close to previous values reported in the literature: 368.2 [30], 367.7 [60], 367.8 [32], and 368.0 eV [61]. Turning to the AgF_2 sample, we find that the binding energy has the expected anomalous negative shift corresponding to a higher oxidation state. The shifts amount to -0.8 eV corresponding to a binding energy of 367.4 eV in good agreement with Refs. [60] (367.3 eV), [32] (367.3 eV), and [30] (367.8 eV). This suggests that the part of the sample under examination is indeed AgF_2. On the other hand, for a d^9 ground state, one expects satellites to appear in the core-level spectra as for the Cu $2p_{3/2}$ level of CuO (see Ref. [29]).
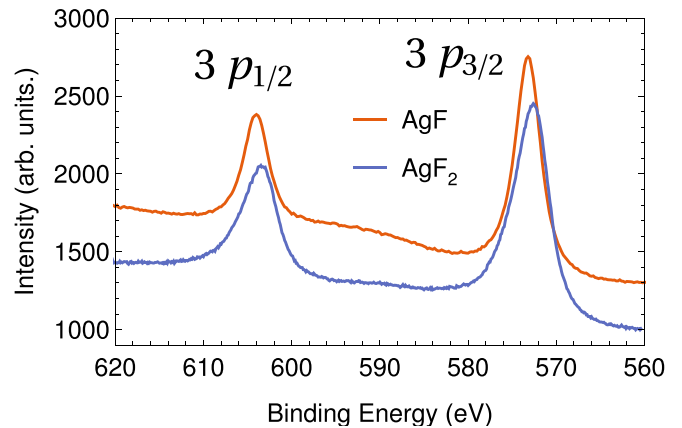
Although the AgF_2 spectrum shows broadening and asymmetry, the satellites do not appear.

Such satellites are not visible in the $3p$ core-level spectra of AgF_2 either (Fig. 11). The absence of satellites in core-level spectra agrees with Ref. [32].

Figure 11 shows the core-level spectra of the $3p$ doublet of both materials. We find a -0.5 chemical shift increasing the oxidation state, which coincides with the shift reported in Ref. [32]. The present binding energy for $3p_{3/2}$ is 572.6 eV, slightly larger than their value (572.0 eV) probably because of small differences in charging corrections.

For completeness, we report the experimental valence band binding energy with the same C $1s$ referencing and measured at the peak maximum. For AgF we find that the binding energy is 5.1 eV compared with 4.8 [32] and 5.26 eV [30]. For AgF_2, we find a binding energy of 4.4 eV compared with 4.4 [32] and 4.9 eV [30].

Overall, we find good agreement with the existing literature for chemical shifts and absolute binding energies, which points to a nominal d^9 ground state in the region of the AgF_2 sample examined. On the other hand, the absence of satellites is puzzling and needs further investigation, for example, by changing the surface preparation conditions.

[1] M. R. Norman, Rep. Prog. Phys. **79**, 074502 (2016).

[2] D. Li, K. Lee, B. Y. Wang, M. Osada, S. Crossley, H. R. Lee, Y. Cui, Y. Hikita, and H. Y. Hwang, Nature (London) **572**, 624 (2019).

[3] It is worth noticing that a large superexchange has been measured in the related overdoped trilayer compound $La_4Ni_3O_8$; see J. Q. Lin, P. Villar Arribi, G. Fabbris, A. S. Botana, D. Meyers, H. Miao, Y. Shen, D. G. Mazzone, J. Feng, S. G. Chiuzbaian *et al.*, Phys. Rev. Lett. **126**, 087001 (2021).

[4] A. S. Botana and M. R. Norman, Phys. Rev. X **10**, 011024 (2020).

[5] A. S. Botana, F. Bernardini, and A. Cano, J. Exp. Theor. Phys. **132**, 618 (2021).

[6] L. H. Tjeng, M. B. J. B. Meinders, J. van Elp, J. Ghijsen, G. A. Sawatzky, and R. L. Johnson, Phys. Rev. B **41**, 3190 (1990).

[7] W. Grochala and R. Hoffmann, Angew. Chem., Int. Ed. **40**, 2742 (2001).

[8] J. Gawraczyński, D. Kurzydłowski, R. A. Ewings, S. Bandaru, W. Gadomski, Z. Mazej, G. Ruani, I. Bergenti, T. Jaroń, A. Ozarowski, S. Hill, P. J. Leszczyński, K. Tokár, M. Derzsi, P. Barone, K. Wohlfeld, J. Lorenzana, and W. Grochala, Proc. Natl. Acad. Sci. USA **116**, 1495 (2019).

[9] A. Grzelak, H. Su, X. Yang, D. Kurzydłowski, J. Lorenzana, and W. Grochala, Phys. Rev. Materials **4**, 084405 (2020).

[10] X. Yang and H. Su, Sci. Rep. **4**, 5420 (2015).

[11] X. Yang and H. Su, Sci. Rep. **5**, 15849 (2015).

[12] C. Miller and A. S. Botana, Phys. Rev. B **101**, 195116 (2020).

[13] S. Y. Davydov, Phys. Solid State **63**, 1633 (2021).

[14] N. Bachar, K. Koteras, J. Gawraczynski, W. Trzcinski, J. Paszula, R. Piombo, P. Barone, Z. Mazej, G. Ghiringhelli,

A. Nag, K.-J. Zhou, J. Lorenzana, D. van der Marel, and W. Grochala, Phys. Rev. Research **4**, 023108 (2022)

[15] M. Cini, Solid State Commun. **24**, 681 (1977).

[16] G. A. Sawatzky, Phys. Rev. Lett. **39**, 504 (1977).

[17] A. Grzelak, T. Jaroń, Z. Mazej, T. Michałowski, P. Szarek, and W. Grochala, J. Electron Spectrosc. Relat. Phenom. **202**, 38 (2015).

[18] J. C. Slater and G. F. Koster, Phys. Rev. **94**, 1498 (1954).

[19] L. Hozoi, L. Siurakshina, P. Fulde, and J. van den Brink, Sci. Rep. **1**, 65 (2011).

[20] H.-Y. Huang, N. A. Bogdanov, L. Siurakshina, P. Fulde, J. van den Brink, and L. Hozoi, Phys. Rev. B **84**, 235125 (2011).

[21] H. Eskes, L. H. Tjeng, and G. A. Sawatzky, Phys. Rev. B **41**, 288 (1990).

[22] O. K. Andersen, W. Klose, and H. Nohl, Phys. Rev. B **17**, 1209 (1978).

[23] E. Antonides, E. C. Janse, and G. A. Sawatzky, Phys. Rev. B **15**, 1669 (1977).

[24] D. K. G. de Boer, C. Haas, and G. A. Sawatzky, Phys. Rev. B **29**, 4401 (1984).

[25] M. B. J. Meinders, J. van den Brink, J. Lorenzana, and G. A. Sawatzky, Phys. Rev. B **52**, 2484 (1995).

[26] J. van den Brink, M. B. J. Meinders, J. Lorenzana, R. Eder, and G. A. Sawatzky, Phys. Rev. Lett. **75**, 4658 (1995).

[27] V. J. Emery, Phys. Rev. Lett. **58**, 2794 (1987).

[28] J. Yeh and I. Lindau, At. Data Nucl. Data Tables **32**, 1 (1985).

[29] J. Ghijsen, L. H. Tjeng, J. van Elp, H. Eskes, J. Westerink, G. A. Sawatzky, and M. T. Czyzyk, Phys. Rev. B **38**, 11322 (1988).

[30] W. Grochala, R. G. Egdell, P. P. Edwards, Z. Mazej, and B. Žemva, Chem. Phys. Chem. **4**, 997 (2003).

[31] M. Cini, Solid State Commun. **20**, 605 (1976).

[32] J. T. Wolan and G. B. Hoflund, Appl. Surf. Sci. **125**, 251 (1998).

[33] C. J. Powell, Phys. Rev. Lett. **30**, 1179 (1973).

[34] G. Seibold, F. Becca, and J. Lorenzana, Phys. Rev. Lett. **100**, 016405 (2008).

[35] D. van der Marel and G. A. Sawatzky, Phys. Rev. B **37**, 10674 (1988).

[36] G. A. Sawatzky, I. S. Elfimov, J. Van Den Brink, and J. Zaanen, Europhys. Lett. **86**, 17006 (2009).

[37] H. Eskes and G. A. Sawatzky, Phys. Rev. Lett. **61**, 1415 (1988).

[38] F. C. Zhang and T. M. Rice, Phys. Rev. B **37**, 3759 (1988).

[39] Sometimes this energy gap is defined as the ZR singlet binding energy. Here we refrain from using this terminology as we use "binding energy" with a different meaning.

[40] M. Jiang, M. Berciu, and G. A. Sawatzky, Phys. Rev. Lett. **124**, 207004 (2020).

[41] M. Moretti Sala, V. Bisogni, C. Aruta, G. Balestrino, H. Berger, N. B. Brookes, G. M. de Luca, D. Di Castro, M. Grioni, M. Guarise, P. G. Medaglia, F. Miletto Granozio, M. Minola, P. Perna, M. Radovic, M. Salluzzo, T. Schmitt, K. J. Zhou, L. Braicovich, and G. Ghiringhelli, New J. Phys. **13**, 043026 (2011).

[42] J. P. Falck, A. Levy, M. A. Kastner, and R. J. Birgeneau, Phys. Rev. Lett. **69**, 1109 (1992).

[43] V. I. Anisimov, J. Zaanen, and O. K. Andersen, Phys. Rev. B **44**, 943 (1991).

[44] M. Cococcioni and S. de Gironcoli, Phys. Rev. B **71**, 035105 (2005).

[45] A. K. McMahan, R. M. Martin, and S. Satpathy, Phys. Rev. B **38**, 6650 (1988).

[46] M. S. Hybertsen, E. B. Stechel, M. Schluter, and D. R. Jennison, Phys. Rev. B **41**, 11068 (1990).

[47] G. Kresse and J. Furthmüller, Phys. Rev. B **54**, 11169 (1996).

[48] See also "Calculate U for LSDA+U"; Vaspwiki available at https://www.vasp.at/wiki/index.php/Calculate_U_for_LSDA%2BU.

[49] J. van Elp, H. Eskes, P. Kuiper, and G. A. Sawatzky, Phys. Rev. B **45**, 1612 (1992).

[50] M. Cococcione (private communication).

[51] G. L. Bottger and A. L. Geddes, J. Chem. Phys. **56**, 3735 (1972).

[52] P. Fischer, D. Schwarzenbach, and H. Rietveld, J. Phys. Chem. Solids **32**, 543 (1971).

[53] S. Bandaru, M. Derzsi, A. Grzelak, J. Lorenzana, and W. Grochala, Phys. Rev. Materials **5**, 064801 (2021).

[54] D. Jezierski, A. Grzelak, X. Liu, S. K. Pandey, M. N. Gastiasoro, J. Lorenzana, J. Feng, and W. Grochala, Phys. Chem. Chem. Phys. **24**, 15705 (2022).

[55] J. Ghijsen, L. H. Tjeng, H. Eskes, G. A. Sawatzky, and R. L. Johnson, Phys. Rev. B **42**, 2268 (1990).

[56] L. H. Tjeng, C. T. Chen, J. Ghijsen, P. Rudolf, and F. Sette, Phys. Rev. Lett. **67**, 501 (1991).

[57] H. Eskes and G. A. Sawatzky, Phys. Rev. B **44**, 9656 (1991).

[58] P. Połczyński, R. Jurczakowski, A. Grzelak, E. Goreshnik, Z. Mazej, and W. Grochala, Chem. Eur. J. **25**, 4927 (2019).

[59] J. A. McMillan, J. Inorg. Nucl. Chem. **13**, 28 (1960); K. Yvon, A. Bezinge, P. Tissot, and P. Fischer, J. Solid State Chem. **65**, 225 (1986); X. Bao, M. Muhler, Th. Schedel-Niedrig, and R. Schlögl, Phys. Rev. B **54**, 2249 (1996).

[60] S. W. Gaarenstroom and N. Winograd, J. Chem. Phys. **67**, 3500 (1977).

[61] V. K. Kaushik, J. Electron Spectrosc. Relat. Phenom. **56**, 273 (1991).